antagonist for Tie2 receptors expressed on endothelial cells in vitro and in vivo. However, we also unexpectedly found that Ang2 acts as an agonist for Tie2 receptors ectopically expressed on nonendothelial cells (fibroblasts). One possible explanation for these disparate effects is that endothelial cells express an accessory component or components required for Ang2 to act as an antagonist. Tie1, which has no known ligand and is expressed predominantly in endothelial cells, may be such a component, perhaps by undergoing Ang2-induced heterodimerization with Tie2 and thus preventing Tie2 activation; however, preliminary evidence argues against this possibility (*17*). The observation that Ang2 can activate Tie2 on certain cultured cells raises the question of whether this activation occurs in vivo, perhaps in a special subclass of endothelial cells, or in the rare nonendothelial cell types that express Tie2, such as the early cells of the hemopoietic lineage (*11*).

REFERENCES AND NOTES

1. W. Risau, *FASEB J.* **9**, 926 (1995); *Nature* **386**, 671 (1997).
2. J. Folkman, *Nature Med.* **1**, 27 (1995).
3. D. Hanahan and J. Folkman, *Cell* **86**, 353 (1996).
4. T. Mustonen and K. Alitalo, *J. Cell Biol.* **129**, 895 (1995).
5. G. H. Fong, J. Rossant, M. Gertenstein, M. L. Breitman, *Nature* **376**, 66 (1995); F. Shalaby *et al*., *ibid*., p. 62; P. Carmeliet *et al*., *ibid.* **380**, 435 (1996); N. Ferrara *et al*., *ibid.*, p. 439.
6. D. Jackson, O. V. Volpert, N. Bouck, D. I. H. Linzer, *Science* **266**, 1581 (1994).
7. M. S. O'Reilly *et al*., *Cell* **79**, 315 (1994).
8. M. S. O'Reilly *et al*., *ibid.* **88**, 277 (1997).
9. S. Davis *et al*., *ibid.* **87**, 1161 (1996).
10. D. J. Dumont, T. P. Yamaguchi, R. A. Conlon, J. Rossant, M. L. Breitman, *Oncogene* **7**, 1471 (1992); P. C. Maisonpierre, M. Goldfarb, G. D. Yancopoulos, G. Gao, *ibid.* **8**, 1631 (1993); T. N. Sato, Y. Qin, C. A. Kozak, K. L. Audus, *Proc. Natl. Acad. Sci. U.S.A.* **90**, 9355 (1993); H. Schnurch and W. Risau, *Development* **119**, 957 (1993); S. F. Ziegler, T. A. Bird, K. A. Schneringer, K. A. Schooley, P. R. Baum, *Oncogene* **8**, 663 (1993).
11. A. Iwama *et al., Biochem. Biophys. Res. Commun.* **195**, 301 (1993).
12. D. J. Dumont *et al*., *Genes Dev.* **8**, 1897 (1994); T. N. Sato *et al*., *Nature* **376**, 70 (1995).
13. C. Suri *et al*., *Cell* **87**, 1171 (1996).
14. Cloning of Ang2 cDNAs resulted from screening a human fetal lung and a mouse adult uterus cDNA library (both from Clontech) with the full-length mouse ^{32}P-labeled Ang1 cDNA probe at 55° or 65°C (*25*).
15. Mutation of Cys^{245} in Ang1, which is not shared between Ang1 and Ang2, does not alter its agonistic properties. For some experiments, Ang1* (a recombinant version of Ang1 with a modified NH_2-terminus and mutated Cys^{245} that is easier to produce and purify) was used instead of Ang1; for details on expression and purification of Ang1, Ang1*, and Ang2, see S. Davis *et al*., in preparation.
16. J. Partanen *et al*., *Mol. Cell. Biol.* **12**, 1698 (1992).
17. P. C. Maisonpierre *et al*., data not shown.
18. K. K. Hirschi and P. A. D'Amore, *Cardiovasc. Res.* **32**, 687 (1996).
19. J. K. Findlay, *J. Endocrinol.* **111**, 357 (1986); H. S. Phillips, J. Hains, D. W. Leung, N. Ferrara, *Endocrinology* **127**, 965 (1990); D. Shweiki, A. Itin, G. Neufeld, H. Gitay-Goren, E. Keshet, *J. Clin. Invest.* **91**, 2235 (1993); E. Bacharach, A. Itin, E. Keshet, *Proc. Natl. Acad. Sci. U.S.A.* **89**, 10686 (1992).
20. T. M. Schlaeger *et al.*, *Proc. Natl. Acad. Sci. U.S.A.* **94**, 3058 (1997).
21. R. Schweitzer, R. Howes, R. Smith, B.-Z. Shilo, M. Freeman, *Nature* **376**, 699 (1995).
22. V. Cioce *et al*., *J. Biol. Chem.* **271**, 13110 (1996).
23. W. P. Arend, H. G. Welgus, R. C. Thompson, S. P. Eisenberg, *J. Clin. Invest.* **85**, 1694 (1990).
24. M. Vikkula *et al*., *Cell* **87**, 1181 (1996).
25. P. C. Maisonpierre *et al.*, *Science* **247**, 1446 (1990).
26. C.-J. S. Edgell, C. C. McDonald, J. B. Graham, *Proc. Natl. Acad. Sci. U.S.A.* **80**, 3734 (1983).
27. P. C. Maisonpierre, P. F. Jones, S. Davis, G. D. Yancopoulos, in preparation.
28. Probes for mouse embryo sections were 560- and 680-nucleotide (nt) cRNAs extending from 5′ leader sequence to, respectively, codon 165 in mouse Ang1 cDNA and codon 155 in mouse Ang2 cDNA. Probes for rat ovary sections were VEGF, a 141-nt cRNA spanning the last 47 rat VEGF codons (which are shared among most VEGF RNA splice-variants); Ang1, a 773-nt cRNA spanning the last 257 codons of mouse Ang1 cDNA; and Ang2, a 315-nt cRNA spanning codons 380 to 485 in rat Ang2 cDNA.
29. To obtain staged ovulating ovarian tissue, we injected immature (postnatal day 29) female Sprague-Dawley rats (Zivic-Miller) with 5 U of pregnant mare serum gonadotropin (Calbiochem). Rats were killed and ovaries were surgically removed beginning at 56 hours after injection and at 9- to 32-hour intervals thereafter.

30. We thank L. S. Schleifer and P. R. Vagelos for enthusiastic support; M. Goldfarb, M. Wang, R. Rossman, D. Datta, Y. Qing, T. Schlaeger, J. Lawitts, and J. Bruno for their contributions; J. Springhorn for HUCEC cells; and C. Murphy, E. Hubel, C. Rudowsky, and E. Burrows for graphics work. T.N.S. was partly supported by Hoffmann–LaRoche Inc.

7 March 1997; accepted 13 May 1997

Crystal Structure of the Cytochrome bc_1 Complex from Bovine Heart Mitochondria

Di Xia, Chang-An Yu, Hoeon Kim, Jia-Zhi Xia, Anatoly M. Kachurin, Li Zhang, Linda Yu, Johann Deisenhofer*

On the basis of x-ray diffraction data to a resolution of 2.9 angstroms, atomic models of most protein components of the bovine cytochrome bc_1 complex were built, including core 1, core 2, cytochrome b, subunit 6, subunit 7, a carboxyl-terminal fragment of cytochrome c_1, and an amino-terminal fragment of the iron-sulfur protein. The positions of the four iron centers within the bc_1 complex and the binding sites of the two specific respiratory inhibitors antimycin A and myxothiazol were identified. The membrane-spanning region of each bc_1 complex monomer consists of 13 transmembrane helices, eight of which belong to cytochrome b. Closely interacting monomers are arranged as symmetric dimers and form cavities through which the inhibitor binding pockets can be accessed. The proteins core 1 and core 2 are structurally similar to each other and consist of two domains of roughly equal size and identical folding topology.

Ubiquinol–cytochrome c oxidoreductase (bc_1 complex) is a component of the eukaryotic or bacterial respiratory chain and of the photosynthetic apparatus in purple bacteria. In mitochondria, this enzyme catalyzes electron transfer from ubiquinol to cytochrome c, which is coupled to the translocation of protons across the mitochondrial inner membrane from the matrix space (negative or N side) to the intermembrane space (positive or P side). Thus, bc_1 contributes to the electrochemical proton gradient that drives adenosine triphosphate (ATP) synthesis (*1*). The purified mitochondrial bc_1 complex contains 11 protein subunits (*2*, *3*); it consists of 2165 amino acid residues and four prosthetic groups with a total molecular mass of 248 kD. The amino acid sequences of all subunits are known; some of them were determined by peptide sequencing (*4*) and others were deduced from nucleotide sequences (*5*). The essential redox components of bc_1 are the two b-type hemes b_L (also called b_{565}) and b_H (b_{562}), one c-type heme (c_1), one high-potential iron-sulfur cluster (2Fe-2S Rieske center), and ubiquinone.

On the basis of functional data (*1*), the proton-motive Q cycle has been favored as a model for bc_1 function (*6*). The key feature of the model is that there are two separate ubiquinone or ubiquinol binding sites; ubiquinol is oxidized at site Q_o, near the P side of the inner mitochondrial membrane, and ubiquinone is reduced at site Q_i, near the N side of the membrane. According to the Q cycle model, one electron is transferred from ubiquinol to the Rieske

D. Xia, H. Kim, and J. Deisenhofer are in the Howard Hughes Medical Institute and Department of Biochemistry, University of Texas Southwestern Medical Center, Dallas, TX 75235, USA. C.-A. Yu, J.-Z. Xia, A. M. Kachurin, L. Zhang, and L. Yu are in the Department of Biochemistry and Molecular Biology, Oklahoma State University, Stillwater, OK 74078, USA.

*To whom correspondence should be addressed. E-mail: jd@howie.swmed.edu

Table 1. Summary of data collection, data statistics, and MIR phasing. Large cell dimensions and weak diffraction of bc_1 complex crystals made data collection with laboratory x-ray sources impractical. All diffraction data were collected on imaging plates at synchrotrons. The images were indexed and reflections were integrated, scaled, and postrefined with the programs DENZO and SCALEPACK (*35*). Screening for possible heavy-atom derivatives yielded two derivatives with good phasing powers and Cullis *R* factors and five derivatives with medium phasing powers and Cullis *R* factors. Programs from the CCP4 package (*36*) were used for merging and scaling heavy-atom derivative data with native data (programs MTZUTILS and SCALEIT), difference-Patterson calculations (program FFT), and heavy-atom parameter refinement (program MLPHARE). Density modification on the MIR map was performed with the program DM (*37*), and the program SIGMAA (*38*) was used in phase combination. Atomic models were built with the program O (*39*). Details of the exact structure remain to be determined by crystallographic refinement. $R_{merge} = \Sigma(|I - \langle I \rangle|)/\Sigma(I)$; $\langle I/\sigma \rangle$, mean intensity–mean rmsd ratio; ⟨PP⟩, mean phasing power; $\langle R_c \rangle$, mean Cullis *R* factor.

Crystal	Resolution (Å)	Completeness (%)		Observations (*N*)		R_{merge} (%)	$\langle I/\sigma \rangle$	⟨PP⟩	$\langle R_c \rangle$	Reflections used (*N*)	Sites (*N*) (including Fe)
		Overall	Last shell	Overall	Unique						
Native	2.9	90.6	62.4	2,166,501	72,196	14.5	10.4	–	–	–	
$(Me)_3PbAc$	3.3	77.6	79.9	403,632	42,507	11.9	9.3	0.88	0.85	39,915	11
$(Me)_3PbCl$	3.4	53.5	21.1	888,158	30,787	17.0	8.6	0.68	0.93	25,582	9
$MeHgPO_4$	3.7	81.4	31.9	235,264	31,793	6.8	21.9	2.30	0.57	28,153	26
$HgCl_2$	3.4	75.2	40.6	775,342	44,982	12.8	10.6	0.50	0.94	36,686	16
K_2PtCl_4	3.0	89.4	89.7	1,308,534	64,435	11.5	8.0	0.70	0.90	38,285	13
$K_2Pt(NO_3)_2$	3.7	90.4	32.9	257,567	35,268	9.3	9.2	0.53	0.93	31,453	11
K_2PtCl_4	3.7	73.1	19.3	595,440	28,831	10.5	9.7	0.33	0.98	14,337	7
Iron edge*	3.3	74.3	55.7	601,180	43,969	9.8	12.7	0.01	0.98†	32,524	4
Resolution (Å)	17.4	11.1	8.2	6.4	5.3	4.5	4.0	3.5	Total		
Reflections (*N*)	358	1149	2283	3805	5690	7956	10,636	13,602	45,479		
Figure of merit	0.8259	0.8589	0.8421	0.8295	0.7484	0.6127	0.4577	0.2063	0.5094		

*Native data set collected at iron atom absorption edge of bc_1 complex crystal ($\lambda = 1.74$ Å). †Anomalous Cullis *R* factor.

iron-sulfur center, and subsequently to cytochrome c_1 and cytochrome c. The newly generated reactive ubisemiquinone then reduces the low-potential cytochrome b heme (b_L). The reduced b_L rapidly transfers an electron to the high-potential cytochrome b heme (b_H), which is located near the opposite side of the membrane. A ubiquinone or ubisemiquinone bound at the Q_i site then oxidizes the reduced b_H. Proton translocation is the result of deprotonation of ubiquinol at the Q_o site and protonation of the reduced ubiquinone at the Q_i site. Ubiquinol generated at the Q_i site is reoxidized at the Q_o site. The Q cycle mechanism is supported by experimental evidence for the oxidant-induced reduction of cytochrome b (*7*), the existence of antimycin-sensitive and -insensitive transient ubisemiquinone radicals (*8*), the ejection of two protons per electron transfer in bc_1 complexes from many sources (*9*), and the binding of specific inhibitors to sites Q_i or Q_o.

In addition to the redox-active components, mitochondrial bc_1 complexes also carry two so-called core proteins, which are not present in bacterial bc_1 complexes and therefore have long been assumed to have structural rather than functional roles. Stable mitochondrial bc_1 cannot be obtained in the absence of the core proteins, whose presence may contribute to the increased stability and higher activity of mitochondrial as compared to bacterial bc_1 complexes.

To better understand the architecture and the reaction mechanisms of the bc_1 complex, we need a detailed atomic model. Recently, bc_1 from bovine heart mitochondria has been crystallized (*10, 11*). We now report the first results of our x-ray crystallographic studies of this complex; we emphasize general features and the location of the redox centers as well as the structures of cytochrome b and of the core proteins, and discuss functional implications.

Structure determination and overview. The bovine bc_1 complex was purified and crystallized as described (*11, 12*). The crystals have the symmetry of space group $I4_122$ with unit cell dimensions of $a = b = 153.5$ Å and $c = 597.7$ Å, and one bc_1 monomer in the crystallographic asymmetric unit; each monomer consists of 11 different subunits (*13*). The best bc_1 crystals diffracted x-rays to 2.9 Å, but loss of high-resolution diffraction indicated considerable radiation damage within a few minutes of exposure at room temperature. Crystals flush-frozen with liquid propane at high concentrations of glycerol maintained their diffraction quality and permitted data collection at beamline X12B of the National Synchrotron Light Source (NSLS) for at least 12 hours without significant decay. Frozen crystals diffracted to 2.6 Å at the high-brilliance beamline BL-4 of the European Synchrotron Radiation Facility (ESRF) but suffered significant radiation damage within less than 1 hour of exposure. Crystals grown in the presence of the respiratory inhibitors antimycin A and myxothiazol were isomorphous with native crystals and were similar in diffraction quality and radiation sensitivity.

We collected two native data sets, one at 1.5 Å and another at 1.74 Å, which is the iron atom absorption edge in the crystal (*14*). For phase determination by multiple isomorphous replacement (MIR) (*15*), we used seven derivative data sets and contributions from the anomalous scattering of the iron atoms from both native and derivative crystals (Table 1). Density modification, which was done taking advantage of the 65% solvent content in the crystals, improved the quality of the electron density maps and permitted chain tracing and polyalanine model building in most of the core and transmembrane regions of the molecule. We further refined the heavy-atom parameters using phases after density modification, and then combined the new MIR phases with phase information from partial polyalanine models to calculate a new map. This procedure was executed iteratively, with each cycle producing a better electron density map. The phase information thus obtained was used to calculate difference maps and anomalous difference maps, giving locations of bound inhibitors and of the iron atoms in the crystal.

On the basis of the electron density map at 2.9 Å resolution, we could assign amino acid sequences to the following protein components of the bc_1 complex: core 1 (445 residues), core 2 (420 residues), cytochrome b (378 residues), subunit 6 (103 residues), subunit 7 (70 residues), parts of cytochrome c_1 (60 of 241 residues), and, tentatively, parts of the iron-sulfur protein (ISP) (62 of 196 residues). Including additional polyalanine models, we have been able to build nearly 1900 residues (about 14,000 non-hydrogen atoms); these ac-

count for about 86% of all the residues in the bc_1 complex (Fig. 1A).

Biochemical studies (*3*) defined the location of the bc_1 subunits with respect to the mitochondrial inner membrane. Accordingly, more than half of the molecular mass of the complex, and also its widest part, extends 75 Å from the membrane-spanning region into the mitochondrial matrix (Fig. 1B). This region consists primarily of core 1, core 2, subunit 6, part of subunit 7, and further unassigned electron density. On the opposite side of the membrane-spanning region, major parts of both cytochrome c_1 and the ISP extend 38 Å into the intermembrane space. The membrane-spanning region itself is ~42 Å thick with 13 transmembrane helices in each bc_1 monomer.

Two bc_1 complex monomers interact in the crystal to form a dimer around a crystallographic twofold symmetry axis (Fig. 1B). The dimeric bc_1 complex is pear-shaped with a maximal diameter of 130 Å and a height of 155 Å, similar to the dimensions observed by electron microscopic studies (*16*). The core 2 and cytochrome b subunits contribute major dimer interactions across the twofold symmetry axis. Subunit 6 interacts with cytochrome b of one monomer and with core 1 and core 2 of the other monomer. The dimeric form of bc_1 has been observed by chromatography and by electron microscopy. It is unknown whether the monomers in the bc_1 dimer cooperate (*17*). A monomeric form of the bc_1 complex has been isolated in the presence of a high concentration of detergents (*17*), but under the conditions of activity assays the complex is most likely in the dimeric state.

In the crystal, the transmembrane regions of neighboring molecules form planes normal to the crystallographic 4_1 axis, stacked on top of each other with alternating orientations of dimeric bc_1 complexes. Most crystal contacts are made by the core 2 subunits in the matrix regions of the molecule, with a few additional contacts by the transmembrane helix region; no contacts are made by the proteins that extend into the intermembrane space. This distribution of crystal contacts between bc_1 dimers is correlated with (and could be in part responsible for) the nonuniform quality

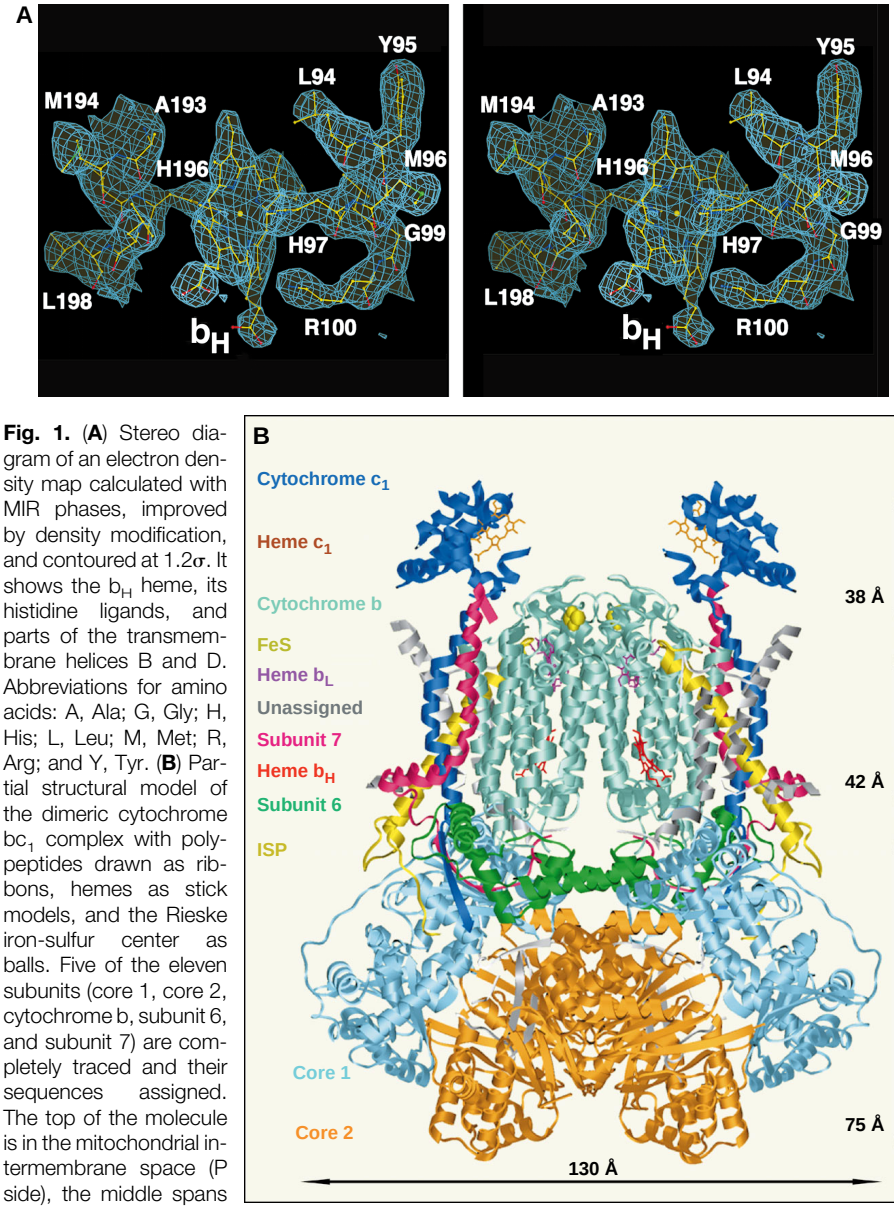

Fig. 1. (**A**) Stereo diagram of an electron density map calculated with MIR phases, improved by density modification, and contoured at 1.2σ. It shows the b_H heme, its histidine ligands, and parts of the transmembrane helices B and D. Abbreviations for amino acids: A, Ala; G, Gly; H, His; L, Leu; M, Met; R, Arg; and Y, Tyr. (**B**) Partial structural model of the dimeric cytochrome bc_1 complex with polypeptides drawn as ribbons, hemes as stick models, and the Rieske iron-sulfur center as balls. Five of the eleven subunits (core 1, core 2, cytochrome b, subunit 6, and subunit 7) are completely traced and their sequences assigned. The top of the molecule is in the mitochondrial intermembrane space (P side), the middle spans the membrane, and the bottom is in the matrix (N side); approximate dimensions are given for each region.

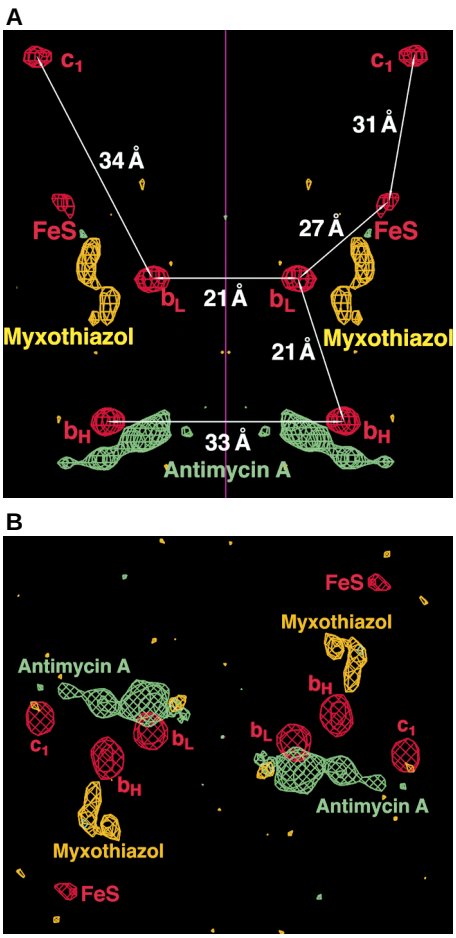

Fig. 2. Anomalous scattering difference–Fourier map contoured at 5.1σ (red) and difference densities between inhibitor-bound and native crystals contoured at 4.5σ (antimycin A) and 4.0σ (myxothiazol). (**A**) View parallel to the membrane plane, with the intermembrane space at the top and the matrix space at the bottom. Peaks were assigned to hemes b_H, b_L, and c_1 and to the Rieske iron-sulfur cluster, respectively, as shown. Distances between some iron pairs are indicated (see Table 2). The twofold symmetry axis of the bc_1 dimer (purple line) runs in the plane of the diagram. (**B**) View perpendicular to the membrane plane.

of the electron density; the quality is highest for the matrix region and lowest for the intermembrane space region, and could reflect differences in crystalline order between these regions.

The model for the extramembrane regions of cytochrome c_1 is in several fragments; only the sequence of the COOH-terminal transmembrane helix has been assigned. Part of the uninterpreted electron density near the c_1 heme may belong to subunit 8, which mediates the contact between cytochrome c_1 and cytochrome c. Despite the compact and rigid structure of the extramembrane domain of the ISP (*18*), the electron density for this domain is particularly poor, indicating that the subunit is highly mobile in the crystal. Mobility could be a functional requirement for electron transfer and might be decreased upon binding of some inhibitors.

Redox centers and inhibitor binding sites. A difference map based on the anomalous scattering effect in the diffraction data from native crystals showed four strong peaks in the crystallographic asymmetric unit, which were at least eight standard deviations above the mean values of the electron density maps (Fig. 2, A and B). When the x-ray wavelength used in the data collection was shifted to the absorption edge of the iron atoms in the crystal, the heights of these peaks increased, although the noise remained unchanged (Table 2), which indicated that the anomalous scattering signal did indeed come from the iron atoms in the bc_1 crystal (as we assumed). Two of these peaks are located in the transmembrane region, one near the matrix (N side) surface and one near the intermembrane space (P side) surface; the other two peaks reside in the intermembrane space region. On the basis of known biochemical and biophysical data (*19–22*), we assigned the two peaks inside the membrane to heme irons of b_L and b_H, respectively, with b_L closer to the P side. One peak in the intermembrane space lies near the P-side membrane surface and most likely represents the iron-sulfur cluster, because it is closer to b_L. The remaining peak must be the heme iron of cytochrome c_1.

The assignment of the iron sites was further supported by binding studies with two specific inhibitors (Fig. 2, A and B). Antimycin A specifically blocks electron flow from heme b_H to ubiquinone. In the difference density map between antimycin A–bound and native crystals, a well-defined feature with the shape of antimycin A appeared in a pocket in the transmembrane region of cytochrome b next to the b_H iron site (Figs. 2 and 3A). There is also extended negative density close to the density of antimycin A, which could represent part of a ubiquinone molecule that is bound in the native crystal but is displaced by bound antimycin A. This suggests that the antimycin A binding site partly overlaps the quinone reduction site Q_i. Mutations in cytochrome b that influence the Q_i site involve residues lining the wall of the antimycin A binding pocket (*23*).

Myxothiazol stops the electron flow from ubiquinol to the iron-sulfur center, and, indirectly, also to b_L. The difference map between myxothiazol-bound and native crystals showed a well-fitting density in a pocket within cytochrome b, midway between the iron positions of b_L and the iron-sulfur center (Figs. 2 and 3B). The myxothiazol binding pocket is underneath the cd helices of cytochrome b, and mutations in these helices lead to a loss of quinol oxidation (*23*). Thus, the myxothiazol binding site is likely to be the quinol oxidation site Q_o of the bc_1 complex. Unlike the Q_i site, this site is not in direct contact with either the b_L heme or the iron-sulfur cluster; it is surrounded by aromatic residues that could mediate electron transfer.

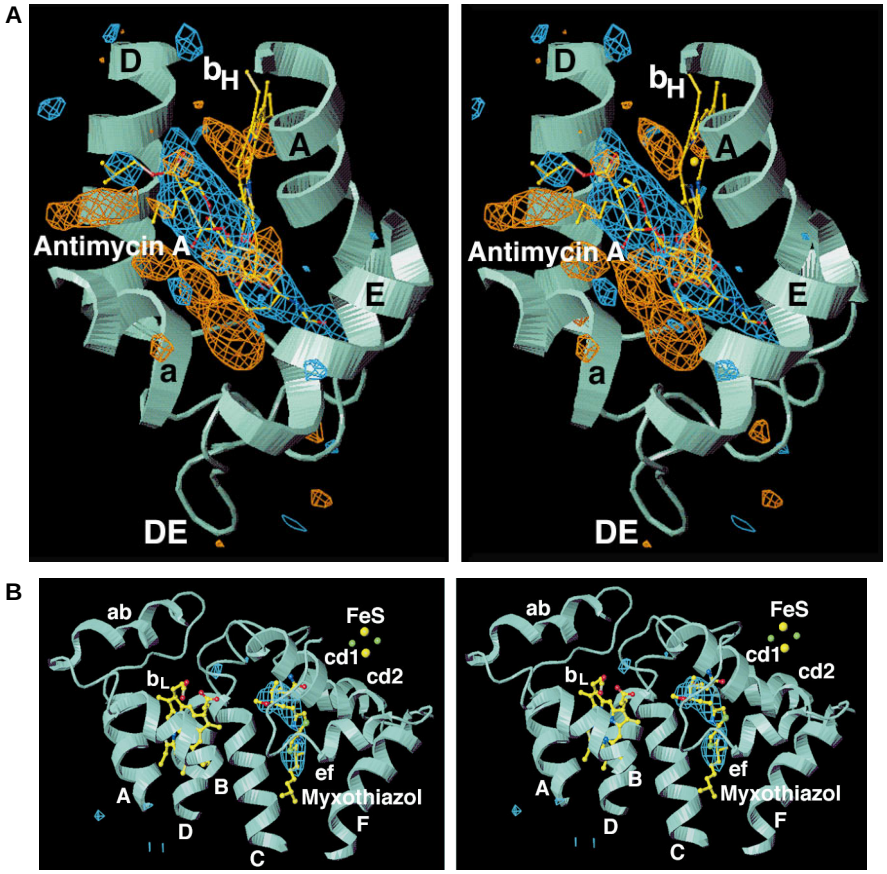

Fig. 3. Inhibitor binding sites in the cytochrome bc_1 complex. (**A**) Stereo diagram of the antimycin A binding pocket. The helices a, A, D, and E of cytochrome b form the pocket as shown. The DE loop is the bottom, and the b_H heme (yellow ball-and-stick model) is the back wall of the pocket. The difference density between inhibitor-bound and native crystals is contoured at 4.5σ (blue) and at –4.5σ (brown). An antimycin molecule is fitted to the positive density. (**B**) Stereo diagram of the myxothiazol binding pocket, formed by helices C, F, cd1, and ef of cytochrome b, as indicated. The b_L heme (yellow ball-and-stick model) and the Rieske iron-sulfur center (green and yellow dots) are about equally distant from the pocket. The difference density is contoured at 4.0σ (blue).

Table 2. Strength of anomalous scattering signals of the irons in bc_1 crystals at two different x-ray wavelengths, and distances between the iron centers. For peak heights, σ is the rmsd from the mean; the next highest peak is ~5σ for both wavelengths. The distances in the upper triangle of the matrix table (italic numbers) are between irons in two different monomers; the distances in the lower triangle are within one monomer.

	Iron centers			
	b_H	b_L	FeS	c_1
Peak heights (σ)				
λ = 1.50 Å	15.5	11.7	9.6	8.0
λ = 1.74 Å	20.7	16.9	11.1	9.7
Distance matrix (Å)				
b_H	*33*	*33*	*54*	*66*
b_L	21	*21*	*40*	*48*
FeS	35	27	*53*	*55*
c_1	51	34	31	*61*

The distances between heme irons in b_H, b_L, c_1, and the iron-sulfur cluster (IS) are listed in Table 2. The angle IS-b_L-b_H is 95°, the angle c_1-IS-b_L is 61°, and the angle c_1-b_L-b_H is 155°. The distance of 21 Å between the two b-type hemes inside the membrane is in good agreement with the prediction of 22 Å from the distance between the putative heme ligands in the primary sequence (*19*) and of the spin relaxation of b_H and b_L in electron paramagnetic resonance (EPR) studies (*21*). The distance of 31 Å between the iron-sulfur cluster and the c_1 heme iron is longer than that expected for the observed high electron transfer rate (*24, 25*). This distance could be bridged by protein chains between the two centers, a major conformational change between oxidized and reduced forms of the ISP, or both. The position of the cytochrome b heme pair inside the membrane is generally in agreement with conclusions drawn from electrochromic (*20*), EPR (*26, 27*), and induced potential measurements (*22*). Some of the distances between iron atoms in different monomers of the dimer, especially between the two b_L's and b_H's, are as short as the distances within one bc_1 monomer (Fig. 2A and Table 2) and appear short enough to allow electron transfer.

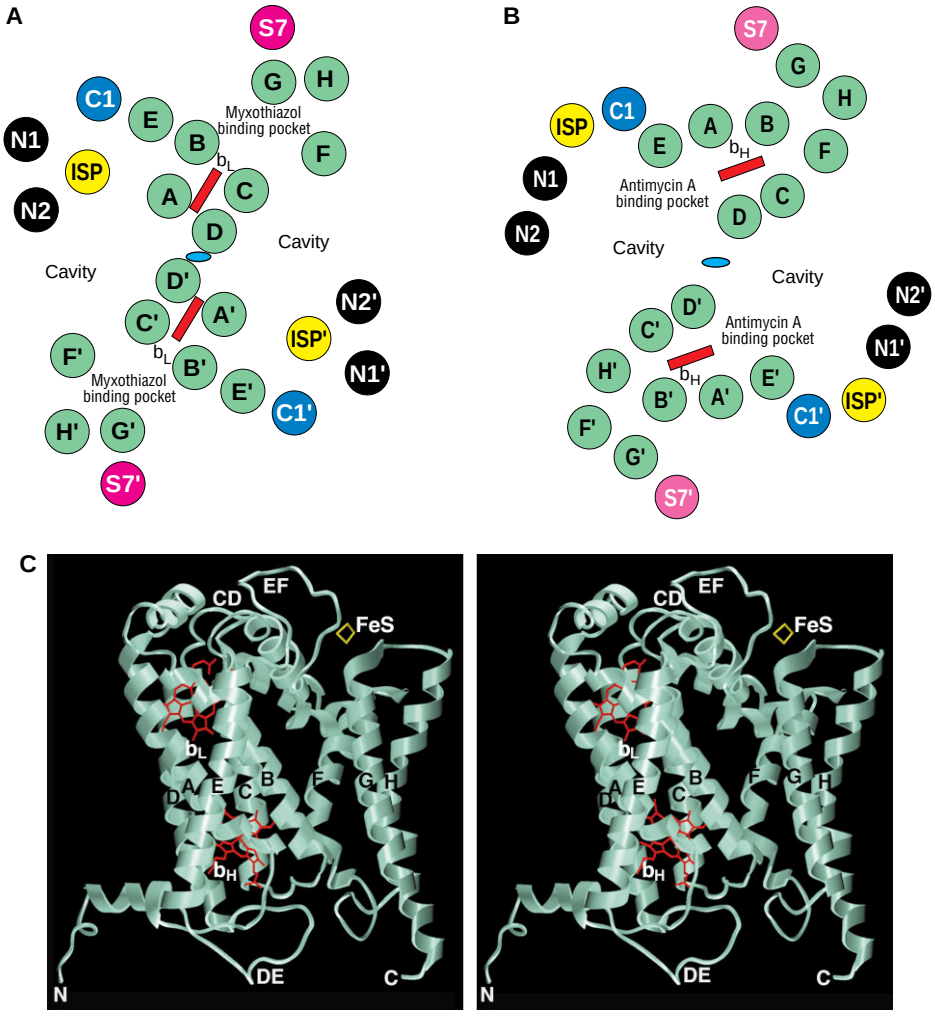

Fig. 4. Membrane-spanning region and cytochrome b. (**A**) Arrangement of the transmembrane helices (represented by circles) of the bc_1 dimer on the P side of the membrane. Green, cytochrome b; blue, cytochrome c_1; magenta, subunit 7; yellow, ISP; black, unassigned; red rectangles, hemes; blue oval, twofold symmetry axis. The eight transmembrane helices of cytochrome b form two groups consisting of helices A to E and F to H, with the myxothiazol binding site in between. The cavity formed by the helices is indicated. Heme b_L is oriented approximately normal to the membrane plane. (**B**) The arrangement of the transmembrane helices on the N side of the membrane [colors as in (A)] is different than on the P side because most of the helices are tilted with respect to the plane of the membrane or have kinks. Heme b_H is oriented approximately normal to the membrane plane and is slightly rotated with respect to heme b_L. The antimycin binding pocket is near heme b_H. (**C**) Stereo diagram of cytochrome b monomer, oriented with the intermembrane space at the top and the matrix at the bottom. The polypeptide chain is represented as a light green ribbon. The eight transmembrane helices are labeled sequentially, A through H. Loops are labeled according to the two helices they connect (loops CD, DE, and EF are labeled as examples). Helices at the membrane surface are denoted a (near NH_2-terminus), ab (in AB loop), cd1 and cd2 (in CD loop), and ef (in EF loop); labels for these helices are not shown. The two groups of transmembrane helices, A to E and F to H, can be distinguished. The hemes, shown in red ball-and-stick models, are bound to helices B and D.

Membrane-spanning region and cytochrome b. There are 13 membrane-spanning helices in the bc_1 monomer structure (Fig. 4, A and B); most of them are tilted with respect to the plane of the membrane. Eight helices, labeled A to H, belong to cytochrome b (Fig. 4C); of the five others, one is the COOH-terminal membrane anchor of cytochrome c_1, one is the COOH-terminal helix of subunit 7, and one is probably the NH_2-terminal membrane anchor of the ISP. The remaining two transmembrane helices are still unassigned; they must belong to subunits 9, 10, or 11. In the bc_1 dimer, the 16 transmembrane helices (8 for each cytochrome b) form the core of the transmembrane helix region, with the other 10 transmembrane helices bound to the periphery. Viewed from either side of the membrane, the overall shape of the bc_1 dimer's transmembrane helix region is approximately elliptical, with long and short axes of ~90 Å and 80 Å, respectively (Fig. 4, A and B).

Both the NH_2- and COOH-termini of the cytochrome b subunit are located in the mitochondrial matrix. The eight transmembrane helices of the cytochrome b subunit are approximately where predicted from hydropathy analysis of the primary sequence and from mutagenesis studies (*28*). They associate into two groups, with helices A, B, C, D, and E in one group and helices F, G, and H in the other (Fig. 4C). The two groups are in close contact on the matrix side and are separated on the intermembrane space side (Fig. 4, A and B). The two b-type hemes are bound within the four-helix bundle made by helices A, B, C, and D. The axial ligands of both hemes are histidines, as predicted (*29*): His^{83} and His^{182} for b_L, and His^{97} and His^{196} for b_H (Fig. 1A). These histidines, located in transmembrane helices B and D, are absolutely invariant in the sequences of b-type cytochromes from more than 900 different species (*19*). Other invariant residues, as well as the sites of inhibitor-resistant mutations (*19*) in cytochrome b, surround the binding sites of myxothiazol and antimycin A.

Topographically, cytochrome b is a rather simple molecule: Four long loops (AB, CD, DE, and EF) and three short loops (BC, FG, and GH) connect the eight transmembrane helices of cytochrome b. The DE loop is on the matrix side, and the other three long loops are on

the intermembrane space side of the membrane. The AB and EF loops each contain one helix. The CD loop has two short helices, named cd1 and cd2, which form a hairpin structure. The extramembrane helices run along the membrane surface, except for helix ef, which is buried inside the membrane. The DE loop does not have any regular secondary structure.

The bc_1 dimer has two large cavities related by the twofold symmetry (Fig. 4, A and B), which are accessible from the membrane bilayer through narrow entrances. The cavities are made of the transmembrane helices D, C, F, and H from one cytochrome b monomer and D′ and E′ from the other monomer, along with the transmembrane helices of c_1, ISP, and two unassigned helices (Fig. 4, A and B). The Q_i pocket of one monomer and the Q_o pocket of the other monomer are accessible through the same cavity. We assume that molecules such as ubiquinol, antimycin A, or myxothiazol can reach their binding sites in the enzyme through these cavities, and that ubiquinol made at the Q_i site can proceed to the nearby Q_o site of the other monomer without having to leave the bc_1 complex. The cavities appear tightly sealed toward the intermembrane space by the surface helices cd1 and cd2 of cytochrome b, but they are solvent-accessible from the matrix side through a channel between core 1, core 2, and subunit 6. This arrangement allows proton uptake at the Q_i site from the matrix and prevents leakage of protons through the bc_1 complex.

Matrix region and core proteins. More than half of the total molecular mass of the bc_1 complex, including the two core proteins, is in the matrix region (*16, 19–22*). Subunit 7 contributes to both the matrix and transmembrane regions. The COOH-terminal 50 residues of subunit 7 form a long, bent transmembrane helix, and the NH_2-terminal part associates with the core 1 protein as part of a β sheet, serving as one of the membrane anchors for the subunits in the matrix region (Fig. 1B). Subunit 6 consists of four helices and connecting loops. It is attached on the matrix side to exposed residues of helices F, G, and H of cytochrome b of one monomer, and it contacts core 1 and core 2 of the other monomer. It has been suggested that this subunit is involved in proton translocation across the inner mitochondrial membrane (*30*), but from our current model it is not obvious how it could serve that function.

The core 1 and core 2 subunits are synthesized in the cytosol as precursor proteins of 480 and 453 amino acid residues, respectively; proteolytic processing in the mitochondrial matrix removes 34 residues from the NH_2-terminus of core 1 and 14 residues from the NH_2-terminus of core 2 (*3*). In our electron density maps, density starts at residue 36 for core 1 and at residue 33 for core 2. Core 1 and core 2 have 21% sequence identity, and their three-dimensional structures are remarkably similar (Fig. 5A). A rotation around an approximate twofold symmetry axis superimposes 384 α-carbon atoms from each subunit with a root mean square deviation (rmsd) of 1.7 Å.

Each of the core subunits consists of two structural domains of about equal size and almost identical folding topology, which are

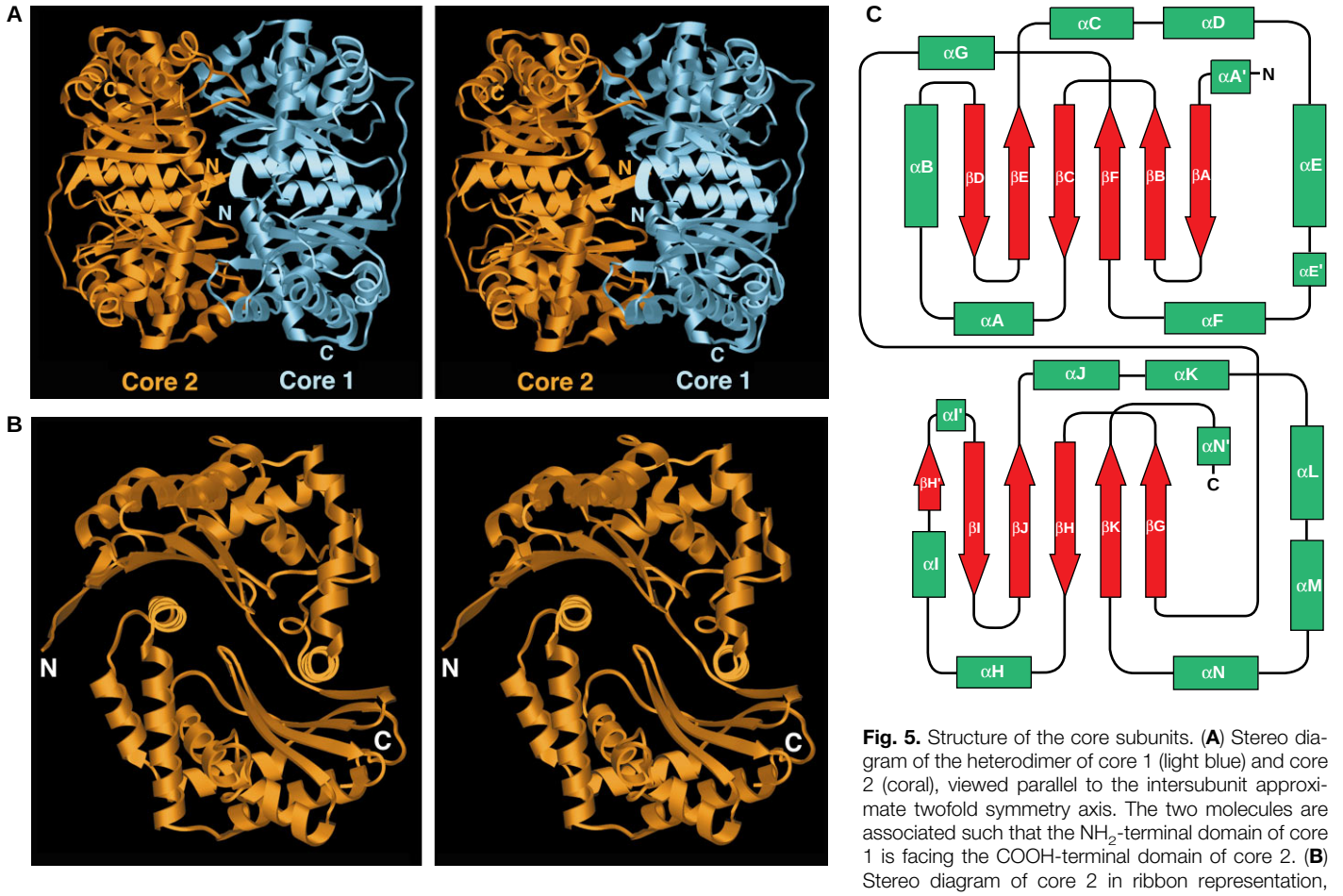

Fig. 5. Structure of the core subunits. (**A**) Stereo diagram of the heterodimer of core 1 (light blue) and core 2 (coral), viewed parallel to the intersubunit approximate twofold symmetry axis. The two molecules are associated such that the NH_2-terminal domain of core 1 is facing the COOH-terminal domain of core 2. (**B**) Stereo diagram of core 2 in ribbon representation, showing two domains of the α-β structure related by an intradomain approximate twofold symmetry axis perpendicular to the plane of the diagram. (**C**) Topology diagram of the core proteins of bc_1. Core 1 and core 2 have similar structures, each clearly separated into an NH_2-terminal domain (top) and a COOH-terminal domain (bottom) with similar folding topology. β strands (red) and α helices (green). The β strand βH′ and α helices αA′, αE′, and αN′ exist only in the core 1 subunit.

also related by approximate twofold rotation symmetry (Fig. 5, B and C). Both domains are folded into one mixed β sheet of six or five β strands, flanked by three α helices on one side and one α helix from the other domain on the other side. Rotation of the COOH-terminal domain on the NH_2-terminal domain superimposes 134 α carbons from each domain of core 1 with an rmsd of 2.0 Å, and 124 α carbons from each domain of core 2 with an rmsd of 2.1 Å. Only about 10% of the superimposed residues are chemically identical. Searches with the program DALI (*31*) did not identify known protein structures closely related to the core subunit domains.

The overall shape of each core protein resembles a bowl (Fig. 5B). In the assembled bc_1 complex, the NH_2-terminal domain of core 1 is interacting with the COOH-terminal domain of core 2, and vice versa (Fig. 5A). Core 1 and core 2 enclose a big cavity that was also observed by electron microscopy (*16*). Because the two internal approximate twofold rotation axes of core 1 and core 2 differ in direction by 14.5°, the two bowls representing these proteins come together in the form of a ball with a crack leading to the internal cavity. The crack is filled with peptide fragments of as yet unknown identity. The amino acid residues lining the wall of the cavity are mostly hydrophilic.

The core proteins of mammalian bc_1 complexes are homologous to the subunits of the general mitochondrial matrix processing peptidase (MPP), which cleaves signal peptides of nucleus-encoded proteins after import into the mitochondrion. MPP belongs to a family of metalloendoproteases whose members include insulin-degrading enzymes from mammals and protease III from bacteria (*32*). Mammalian MPP is a soluble heterodimer of α and β subunits localized in the mitochondrial matrix. Both subunits of MPP are required for the protease activity (*33*), and the active site is part of the β subunit. The core 1 protein of the bovine bc_1 complex has 56% sequence identity to the β subunit of rat MPP, 38% to yeast, and 42% to potato, whereas the core 2 protein is 27% identical to the α subunit of rat MPP, 28% to yeast, and 30% to potato. We can therefore expect that the MPPs of these species are similar in structure to the bovine core 1 and core 2 subunits. In plant mitochondria, the MPP activity is membrane-bound and is an integral part of the bc_1 complex (*34*).

REFERENCES AND NOTES

1. Y. Hatefi, A. G. Haavik, D. E. Griffiths, *J. Biol. Chem.* **237**, 1681 (1962); U. Brandt and B. L. Trumpower, *Crit. Rev. Biochem. Mol. Biol.* **29**, 165 (1994); B. L. Trumpower and R. B. Gennis, *Annu. Rev. Biochem.* **63**, 675 (1994); R. B. Gennis *et al.*, *J. Bioenerg. Biomembr.* **25**, 195 (1993).
2. H. Schägger, T. A. Link, W. D. Engel, G. Von Jagow, *Methods Enzymol.* **126**, 224 (1986).
3. D. Gonzalez-Halphen, M. A. Lindorfer, R. A. Capaldi, *Biochemistry* **27**, 7021 (1988).
4. S. Wakabayashi, H. Takeda, H. Matsubara, C. H. Kim, T. E. King, *J. Biochem. (Tokyo)* **91**, 2077 (1982); S. Wakabayashi *et al., J. Biol. Chem.* **260**, 337 (1985); H. Schägger, U. Borchart, H. Aquila, T. A. Link, G. Von Jagow, *FEBS Lett.* **190**, 89 (1985); H. Schägger, U. Borchart, W. Machleidt, T. A. Link, G. Von Jagow, *ibid.* **219**, 161 (1987); U. Borchart, W. Machleidt, H. Schägger, T. A. Link, G. Von Jagow, *ibid.* **191**, 125 (1985); *ibid.* **200**, 81 (1986).
5. S. Anderson *et al., Nature* **290**, 457 (1981); S. Gencic, H. Schägger, G. Von Jagow, *Eur. J. Biochem.* **199**, 123 (1991); S. Usui, L. Yu, C.-A. Yu, *Biochem. Biophys. Res. Commun.* **167**, 575 (1990); L. Yu, K. P. Deng, C.-A. Yu, *J. Biol. Chem.* **270**, 25634 (1995).
6. P. Mitchell, *J. Theor. Biol.* **62**, 327 (1976); B. L. Trumpower, *J. Biol. Chem.* **265**, 11409 (1990).
7. M. Erecinska, B. Chance, D. F. Wilson, P. L. Dutton, *Proc. Natl. Acad. Sci. U.S.A.* **69**, 50 (1972); M. K. Wikstrom and J. A. Berden, *Biochim. Biophys. Acta* **283**, 403 (1972).
8. C.-A. Yu, S. Nagaoka, L. Yu, T. E. King, *Biochem. Biophys. Res. Commun.* **82**, 1070 (1978); T. Ohnishi and B. L. Trumpower, *J. Biol. Chem.* **255**, 3278 (1980).
9. M. D. Brand, B. Reynafarje, A. L. Lehninger, *J. Biol. Chem.* **251**, 5670 (1976); R. Mitchell, I. C. West, A. J. Moody, P. Mitchell, *Biochim. Biophys. Acta* **849**, 229 (1986); I. C. West, *ibid.,* p. 236.
10. W.-H. Yue, Y.-P. Zou, L. Yu, C.-A. Yu, *Biochemistry* **30**, 2303 (1991); C.-A. Yu, D. Xia, J. Deisenhofer, L. Yu, *J. Mol. Biol.* **243**, 802 (1994); T. Kubota *et al., ibid.* **221**, 379 (1991); E. A. Berry, L. Huang, T. N. Earnest, B. K. Jap, *ibid.* **224**, 1161 (1992); M. Kawamoto *et al., ibid.* **244**, 238 (1994); E. A. Berry, V. M. Shulmeister, L.-S. Huang, S.-H. Kim, *Acta Crystallogr.* **D51**, 235 (1995); J. W. Lee, M. Chan, T. V. Law, H. J. Kwon, B. K. Jap, *J. Mol. Biol.* **252**, 15 (1995).
11. C.-A. Yu *et al., Biochim. Biophys. Acta* **1275**, 47 (1996).
12. Cytochrome bc_1 complex suitable for crystallization was obtained on solubilization of the bc_1 particle by deoxycholate and removal of contaminants by a 15-step ammonium acetate fractionation. The purified complex in the oxidized form was recovered in the precipitates formed between 18.5 and 33.5% saturation of ammonium acetate; it contained 8.3 nmol of cytochrome b, 4.7 nmol of cytochrome c_1, 3.5 nmol of ubiquinone, and 250 nmol of phospholipid per milligram of protein, and gives 10 protein bands in SDS–polyacrylamide gel electrophoresis (PAGE). The specific activity was 11 μmol of cytochrome c reduced per minute per nanomole of cytochrome b at room temperature. For crystallization, purified complex was diluted to a final concentration of 20 mg/ml in 50 mM Mops buffer (pH 7.2), containing 20 mM ammonium acetate, 20% glycerol, and either 0.1% DMG (decanoyl-*N*-methyl-glucamide) or 0.1% SPC (diheptanoyl-phosphatidylcholine). A precipitant solution of 12% polyethylene glycol (PEG, molecular weight 4000) in 50 mM Mops buffer containing 0.5 M KCl, 20% glycerol, and 0.1% detergent was slowly added to the cytochrome bc_1 complex solution with constant stirring until a volume ratio of 0.57:1 (precipitant solution:protein solution) was reached. After incubation for 2 hours at 0°C, the mixture was centrifuged for 10 min at 40,000*g* to remove precipitates. Portions of 30 to 50 μl of clear solution were placed in small test tubes and incubated with 5 ml of equilibrating solution, containing 18% PEG, 0.5 M KCl, and 20 mM tris-Cl buffer (pH 7.0) at 0° to 4°C. Crystals matured in 3 to 4 weeks; they were rectangular in shape and ranged in size from 0.4 to 0.7 mm.
13. K. P. Deng, L. Zhang, C.-A. Yu, unpublished data.
14. W. A. Hendrickson, J. L. Smith, R. P. Phizackerley, E. A. Merritt, *Proteins Struct. Funct. Genet.* **4**, 77 (1988).
15. D. W. Green, V. M. Ingram, M. F. Perutz, *Proc. R. Soc. London Ser. A* **225**, 287 (1954).
16. K. Leonard, P. Wingfield, T. Arad, H. Weiss, *J. Mol. Biol.* **149**, 259 (1981); T. Akiba *et al., Nature Struct. Biol.* **3**, 553 (1996).
17. A. Musatov and N. C. Robinson, *Biochemistry* **33**, 13005 (1994); M. J. Nalecz, R. Bolli, A. Azzi, *Arch. Biochem. Biophys.* **236**, 619 (1985).
18. S. Iwata, M. Saynovits, T. A. Link, H. Michel, *Structure* **4**, 567 (1996).
19. W. R. Widger, W. A. Cramer, R. G. Herrmann, A. Trebst, *Proc. Natl. Acad. Sci. U.S.A.* **81**, 674 (1984); M. Degli Esposti *et al., Biochim. Biophys. Acta* **1143**, 243 (1993).
20. E. G. Glaser and A. R. Crofts, *Biochim. Biophys. Acta* **766**, 322 (1984); D. E. Robertson and P. L. Dutton, *ibid.* **935**, 273 (1988).
21. G. Von Jagow, T. A. Link, T. Ohnishi, *J. Bioenerg. Biomembr.* **18**, 157 (1986).
22. T. Miki, M. Miki, Y. Orii, *J. Biol. Chem.* **269**, 1827 (1994); D. Tolkatchev, L. Yu, C.-A. Yu, *ibid.* **271**, 12356 (1996).
23. G. Brasseur, A. S. Sangas, F. Daldal, *Biochim. Biophys. Acta* **1275**, 61 (1996).
24. H. Ding *et al., Biochemistry* **34**, 15979 (1995).
25. A.-L. T'sai, J. S. Olson, G. Palmer, *J. Biol. Chem.* **258**, 2122 (1983).
26. T. Ohnishi *et al., ibid.* **264**, 735 (1989).
27. J. C. Salerno, M. Osgood, Y. J. Liu, H. Taylor, C. P. Scholes, *Biochemistry* **29**, 6987 (1990).
28. J. P. Di Rago and A.-M. Colson, *J. Biol. Chem.* **263**, 12564 (1988); A. R. Crofts, H. Robinson, K. Andrews, S. Van Doren, E. A. Berry, in *Cytochrome Systems: Molecular Biology and Bioenergetics*, S. Papa, B. Chance, L. Ernster, Eds. (Plenum, New York, 1987), pp. 617–624.
29. C. H. Yun, A. R. Crofts, R. B. Gennis, *Biochemistry* **30**, 6747 (1991).
30. T. Cocco *et al., Eur. J. Biochem.* **195**, 731 (1991).
31. L. Holm and C. Sander, *Science* **273**, 595 (1996).
32. N. D. Rawlings and A. J. Barrett, *Biochem. J.* **275**, 389 (1991).
33. V. Paces, L. E. Rosenberg, W. A. Fenton, F. Kalousek, *Proc. Natl. Acad. Sci. U.S.A.* **90**, 5355 (1993).
34. E. Glaser, A. Eriksson, S. Sjöling, *FEBS Lett.* **346**, 83 (1994); E. Glaser, S. Sjöling, C. Szigyarto, A. C. Eriksson, *Biochim. Biophys. Acta* **1275**, 33 (1996); H.-P. Braun, M. Emmermann, V. Kruft, U. K. Schmitz, *EMBO J.* **11**, 3219 (1992); H.-P. Braun and U. K. Schmitz, *Trends Biochem. Sci.* **20**, 171 (1995).
35. Z. Otwinowski, in *Data Collection and Processing*, L. Sawyer, N. Isaacs, S. Bailey, Eds. (SERC Daresbury Laboratory, Warrington, UK, 1993), pp. 56–62.
36. CCP4, *The SERC (UK) Collaborative Computing Project No. 4, a Suite of Programs for Protein Crystallography* (Daresbury Laboratory, Warrington, UK, 1979).
37. K. D. Cowtan and P. Main, *Acta Crystallogr.* **D52**, 43 (1996).
38. R. J. Read, *ibid.* **A42**, 140 (1986).
39. T. A. Jones, J.-Y. Zou, S. W. Cowan, M. Kjeldgaard, *ibid.* **A47**, 110 (1991).

40. Supported in part by NIH grant GM 30721 (C.A.Y.), the Welch Foundation (J.D.), and the HHMI. The native and derivative data sets were mainly collected at beamline X12B and the multiwavelength anomalous dispersion data at beamline X4A of NSLS at Brookhaven National Laboratory. Exploratory diffraction experiments of the bc_1 complex crystals were performed mainly at beamline 7-A of the Stanford Synchrotron Radiation Laboratory. Beamline 4 of ESRF, beamline 7 of the Cornell High Energy Synchrotron Source, and beamline X8A of NSLS also provided beam time. We thank the staffs of synchrotron facilities in the United States and Europe for help; our colleagues at UT Southwestern Medical Center for their support; S. K. Buchanan and L. Esser for discussions; B. S. Smith, D. B. Staber, and S. Kyle for technical assistance; and K. Fischer Lindahl and C. A. Hasemann for criticism of the manuscript. The coordinates have been deposited in the Brookhaven Protein Data Bank (access number 1QCR).

23 December 1996; accepted 15 May 1997